Supplementary Information (SI) for Nanoscale.
This journal is © The Royal Society of Chemistry 2024

Supporting Information

Carrier type and density dependence of impact ionization characteristics in WSe_2

Haeju Choi[1,2], Jinshu Li[1,2], Taeho Kang[1,2], Sangmin Lee[1,2], Euyheon Hwang[1,2,3], Sungjoo Lee[1,2,3*]*

[1]SKKU Advanced Institute of Nanotechnology (SAINT), Sungkyunkwan University, Suwon 16419, South Korea

[2]Department of Nano Science and Technology, Sungkyunkwan University, Suwon 16419, South Korea

[3]Department of Nano Engineering, Sungkyunkwan University, Suwon 16419, South Korea.

*Corresponding Author E-mail: leesj@skku.edu

Contents

Supplementary Section 1. Fabrication process

a. Fabrication process

b. Image of the WSe_2 flake and device

Supplementary Section 2. Demonstration of impact ionization

a. Electrical characteristics of WSe_2 FETs at low temperatures

b. Reversible output characteristics during V_{DS} sweeps

c. Analysis of impact ionization

d. Dividing region depending on changing slope after impact ionization

e. Reliability of impact ionization phenomenon

Supplementary Section 3. Theoretical analysis of impact ionization

a. Monte Carlo transport simulation

b. Two-dimensional polarizability

c. Scattering rates and probability distributions for other scattering mechanisms

d. Excluding the effect of carrier–carrier scattering

Supplementary Section 4. Photodetection via impact ionization

a. Photo-responsive characteristics based on carrier type

b. Carrier density dependent photodetection

c. Photodetection by optimized impact ionization

d. Parameters for evaluating the performance of APD

Supplementary Section 1. Device fabrication

a. Fabrication process

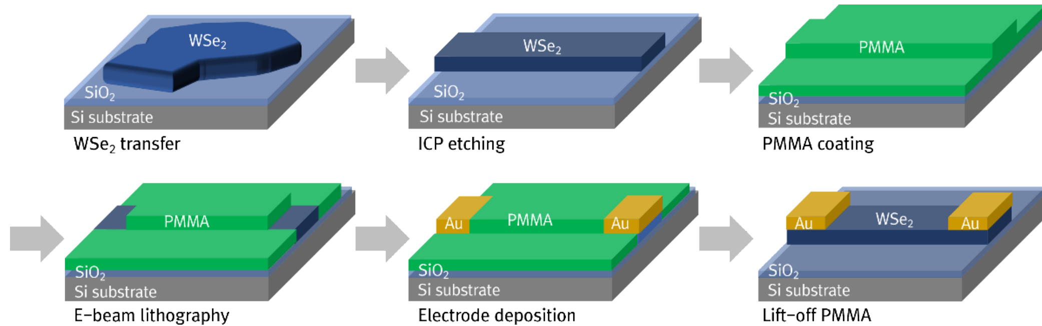

Figure S1. Schematic illustrations of the process flow for the WSe_2 FET fabrication

Figure S1 illustrates the WSe_2 FET fabrication process. To fabricate WSe_2 channel layers, flakes were mechanically exfoliated from a bulk WSe_2 crystal onto a SiO_2/Si substrate. Subsequently, polymethyl methacrylate (PMMA) was spin-coated onto the WSe_2 channels to create double-electron resistor layers. The process involved spinning at 2000 rpm for 5 s at 450 K, followed by 4000 rpm for 35 s at 950 K. Each layer was then baked at 180 °C for 2 min on a hot plate. Following the patterning of the source and drain electrodes using electron beam lithography, Au with a thickness of approximately 50 nm was deposited using an electron beam evaporator to form the source and drain electrodes.

b. Image of the WSe_2 flake and device

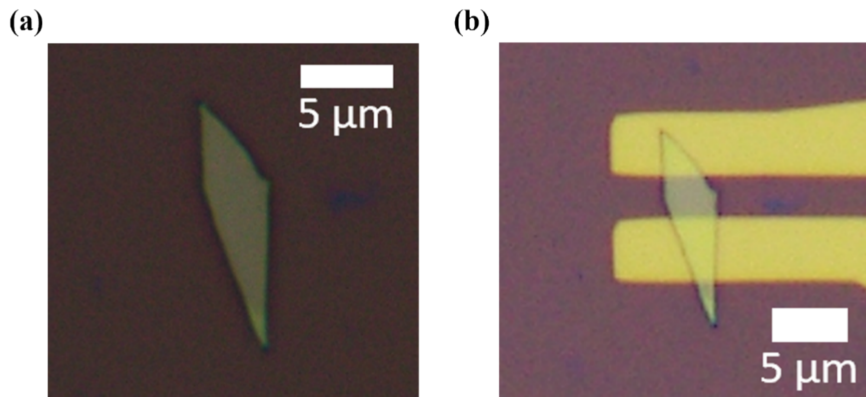

Figure S2. Optical image of the **(a)** exfoliated WSe_2 flake and **(b)** fabricated WSe_2 FET

Figure S2 shows optical images of the exfoliated WSe_2 flake and fabricated WSe_2 FET. The candidate flakes of WSe_2 were selected by color contrast, and their detailed thickness characterization was conducted via atomic force microscopy (AFM) as shown in Fig. 1b. We normally use multilayer flakes with a thickness of approximately 50 nm. The length information of the representative WSe_2 FET is also shown in Fig. 1b.

Supplementary Section 2. Demonstration of impact ionization

a. Electrical characteristics of WSe_2 FETs at low temperatures

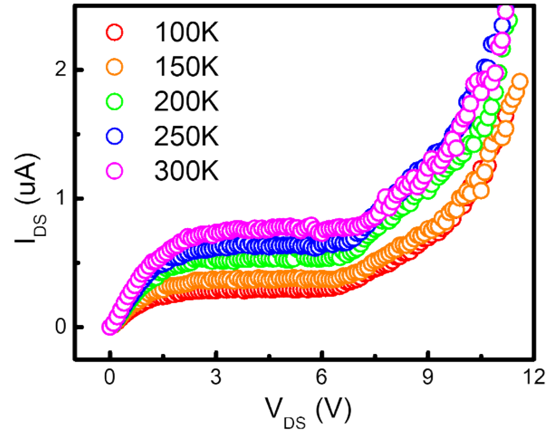

Figure S3. Output curve measured from 100 to 300 K with a step of 50 K.

Figure S3 shows the output characteristics of the WSe_2 FET across a temperature range of 100–300 K. Specifically, I_{DS} and V_{BR} increase with increasing temperature, a behavior commonly associated with thermionic emission. However, the differences beyond the impact ionization threshold are minimal, indicating that the enhancement of the impact ionization characteristics through this range of temperature changes is not substantial.

b. Reversible output characteristics during V_{DS} sweeps

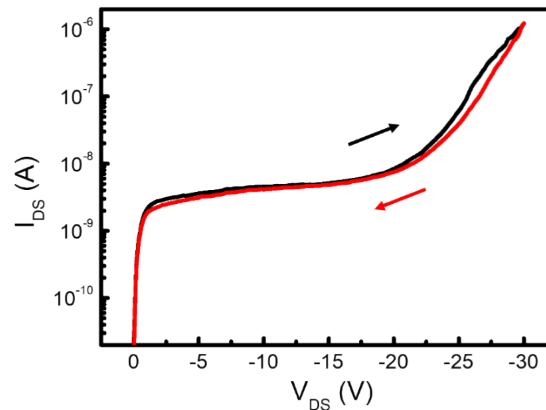

Figure S4. Hysteresis curve of the WSe_2 FETs. Sweep directions are denoted by arrows.

Figure S4 shows the output characteristic of the WSe_2 FET. The output curves, which incorporate

the hole-initiated impact ionization process, were recorded during multiple V_{DS} sweeps. These findings imply that the WSe_2 channel remained intact after undergoing reversible impact ionization without any damage from thermal stress caused by Joule heating.

c. Analysis of impact ionization

To further confirm the impact ionization effect and determine its characteristics in WSe_2, we performed a more detailed analysis of the WSe_2 FET behavior. In line with the theoretical model for the impact ionization effect, when this phenomenon occurs, the multiplication factor M exhibits the following behavior:

$$M = \frac{1}{1 - (\frac{V_{DS}}{V_{BR}})^n} = \frac{1}{1 - (\frac{E}{E_{CR}})^n}$$

where n denotes the index corresponding to the ionization rate. This equation can be expressed in a linear form as follows:

$$\ln\left(1 - \frac{1}{M}\right) = n \times (\ln(E) - \ln(E_{CR}))$$

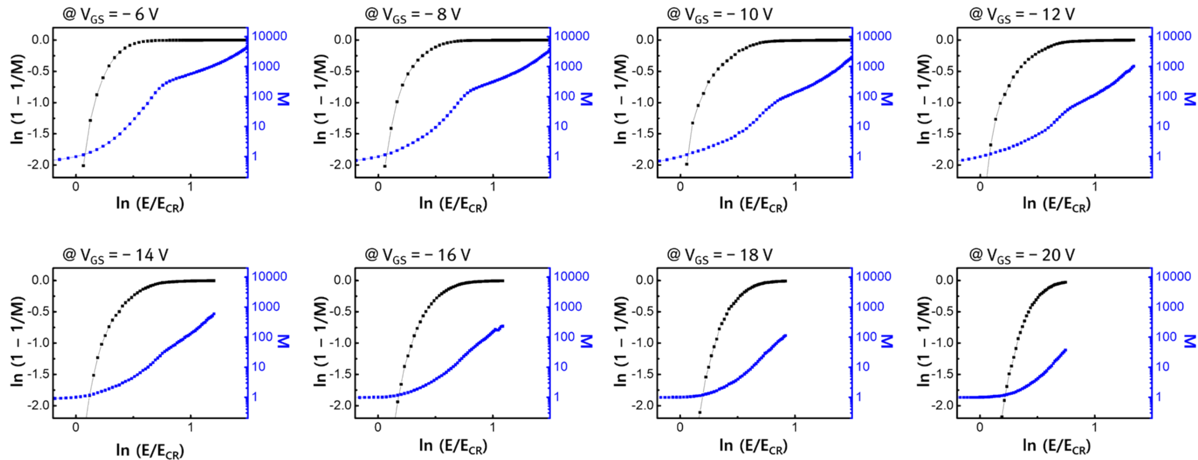

Figure S5. 1-1/M values versus E-field at various values of V_{GS} from –6 V (Charge neutral point) to –20 V.

Figure S5 shows 1-1/M (black symbol) and M (blue symbol) as a function of E/E_{CR} at different

V_{GS} values from –6 V (Charge neutral point) to –20 V. With the increase in carrier density corresponding to an increase in gate voltage, the index n, representing the slope in the low electric field to critical electric field (E/E_{CR}) region, decreases. Moreover, the variation in the slope of the multiplication factor M for E/E_{CR} is consistent with the slope change depicted in Fig. 2f.

d. Dividing region depending on changing slope after impact ionization

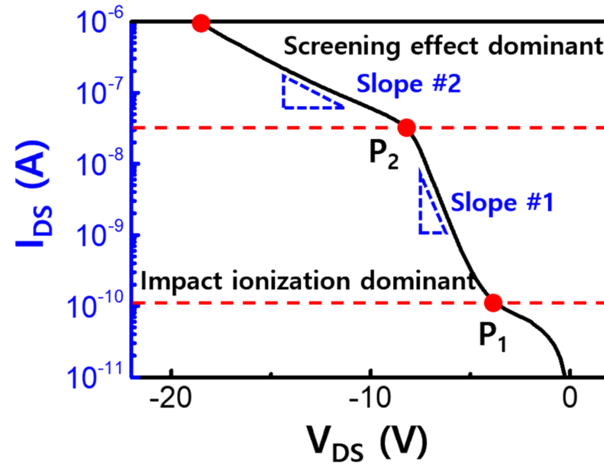

Figure S6. Representative output curve that clearly shows slope ($\Delta I_{DS}/\Delta V_{DS}$) change with increasing applied voltage (at $V_{GS} = V_{CNP} = -6$ V)

Following the onset of impact ionization (P_1), a sharp increase in channel current with a steep slope is observed. However, as the number of generated carriers reaches a certain high value (P_2), the screening effect becomes predominant, leading to a more gradual increase in the current slope. This transition marks the division of the behavior into two distinct regions based on the change in slope (Slope #1: Impact ionization dominant region; Slope #2: Screening effect dominant region).

e. Reliability of impact ionization phenomenon

Figure S7 displays the cumulative probabilities of the breakdown voltage (V_{BR}) derived from cycle-to-cycle data, showcasing results for the same device at various gate voltages across multiple cycles. Even after hundreds of cycles, similar impact ionization characteristics are

observed, indicating that there is no significant degradation apart from minor variations. The reliability of these observations can be quantified using the coefficient of variation (CV), a measure commonly employed to assess the dispersion within probability distributions. The CV can be calculated using the following expression: $CV = (\sigma/\mu) \times 100\ (\%)$, where σ denotes the standard deviation and μ denotes the absolute mean value. Specifically, CV decreases as gate voltage increases because a larger gate voltage confines the path of carrier travel. This, in turn, leads to a stable V_{BR}.

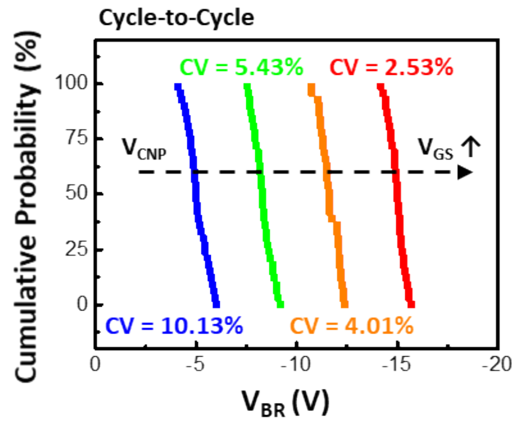

Figure S7. Each V_{BR} during repeated impact ionization process at various applied gate voltages are shown as cumulative probability curves

Supplementary Section 3. Theoretical analysis of impact ionization

a. Monte Carlo transport simulation

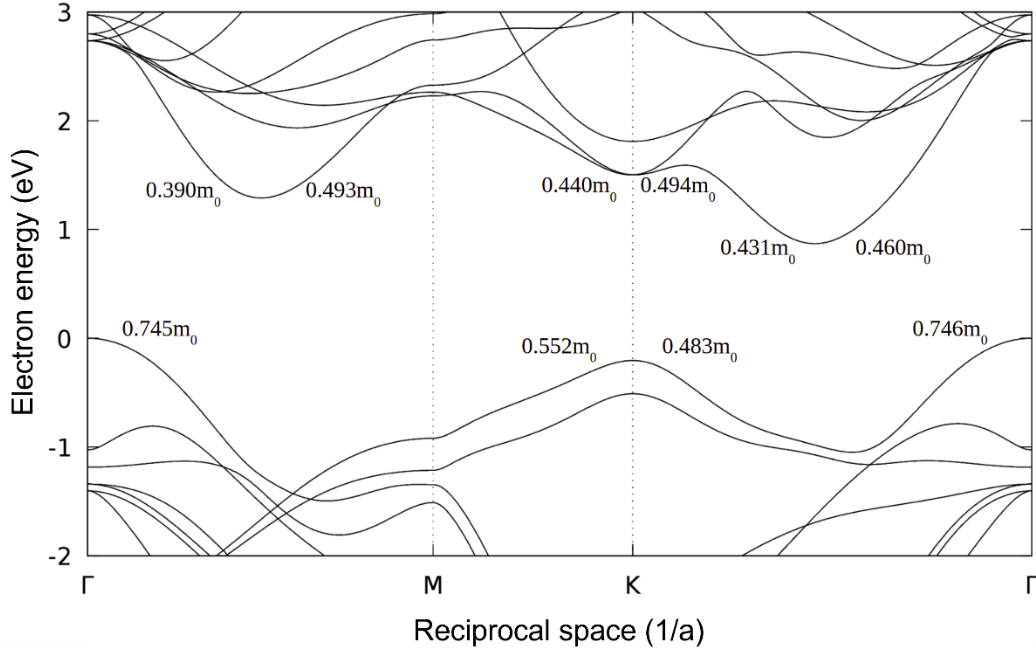

Figure S8. Band structure of multilayer WSe_2 and approximated effective mass

The simple analytical band structure, employing the effective mass approximation, successfully replicates the observed transport phenomena. The breakdown electric field calculations, along with their dependencies on carrier density and temperature, align well with experimental observations. The extended channel length ensures a steady-state behavior for carrier motion in the inversion layer, allowing for the monitoring of its transport using the single-electron Monte Carlo (SMC) method [S1, S2]. We tracked the carrier from collision to collision until it reached a steady state. A carrier that reached the outer boundary was considered to have escaped to the external environment (electrode) and was not tracked further. This approach assumes that the behavior of this carrier is representative of the behavior of the remaining carriers, indicating that the system is ergodic.

For hole transport in the lateral device, we consider the carriers in the inversion layer as a two-dimensional electron gas with a strictly δ function-like distribution in the perpendicular direction. This can be defined as the z direction. Hence, the wave function is as follows:

$$\Psi_k = \delta(z) exp(ik \cdot r), \quad \text{(S1)}$$

where **k** = (k_x, k_y) denotes the two-dimensional wave vector in the plane, and **r**≡ (x,y). The

$$\epsilon(k) = \frac{\hbar^2 k^2}{2m^*}, \quad \text{(S2)}$$

corresponding eigenenergy of the state $\Psi_{\mathbf{k}}$ is as follows:

where $m^* = \sqrt{m_x m_y} = 0.745 m_0$ denotes the hole effective mass of multilayer WSe_2. The corresponding density of states is $\sqrt{\frac{g_s g_v}{4\pi\hbar^2}}$, where $g_s = 2$ denotes the spin degeneracy and $g_v = 1$ denotes the valley degeneracy that the valance band maximum is in Γ point in the Brillouin zone. While a full consideration of the band structures would lead to different predictions for the specific breakdown voltage, we expect a similar breakdown behavior with varying carrier densities. The changes in screening effects with both carrier density and temperature that would be obtained by considering the full-band structure have not yet been investigated.

The dominant input files in the Monte Carlo simulation are the scattering rates determined by various scattering mechanisms. Specifically, for hot carrier transport, they are phonons. Based on Fermi's golden rule, the deterministic carrier scattering rate from a state **k** to a state **k'** is provided

$$W_{\mathbf{kk}'} = \frac{2\pi}{\hbar} |C(q)|^2 \Delta(\epsilon(k), \epsilon(k')), \quad \text{(S3)}$$

by:

where $q = |q| = |k - k'|$, and factor $\Delta(\epsilon(k), \epsilon(k'))$ is as follows:

$$\Delta(\epsilon, \epsilon') = N_q \delta(\epsilon - \epsilon' + \hbar\omega_q) + (N_q + 1)\delta(\epsilon - \epsilon' - \hbar\omega_q)\Theta(\epsilon - \hbar\omega_q) \quad \text{(S4)}$$

where $\hbar\omega_q$ denotes the phonon energy with occupation number $N_q = 1/[\exp(\beta\omega_q) - 1]$. The fir st (second) term in Eq. (S4) corresponds to the absorption (emission) of a phonon. The matrix ele ment $C(q)$ is determined by different phonon scattering mechanisms.

$$|C(q)|^2 = \frac{D^2 \hbar q}{2\rho u_l A}, \quad \text{(S5)}$$

For an acoustic phonon via deformation coupling [S3, S4]:

where D denotes the deformation potential coupling constant, A denotes the area, ρ and u_l denote the mass density and longitudinal sound velocity, respectively.

$$|C(q)|^2 = \frac{2\pi e^2 \omega_0}{qA}\left(\frac{1}{\kappa_\infty} - \frac{1}{\kappa_0}\right), \quad \text{(S6)}$$

For polar LO phonon [S4]:

where $\hbar\omega_0$ = 32 meV (E_g mode) for LO-phonon energy, and κ_∞ denotes the optical dielectric constant, κ_0 denotes the static dielectric constant [S5], and e denotes the electron charge.

For zero order nonpolar optical phonon [S3, S6]:

$$|C(q)|^2 = \frac{D_0^2 \hbar}{2\rho\omega_0 A}, \quad \text{(S7)}$$

where D_0 denotes the deformation-potential coupling constant, and ω_0 denotes the frequency for nonpolar optical phonon.

For first order nonpolar optical phonon [S6]:

$$|C(q)|^2 = \frac{D_1^2 \hbar q^2}{2\rho\omega_0 A}, \quad \text{(S8)}$$

where D_1 denotes the deformation-potential coupling constant, and ω_0 denotes the frequency for nonpolar optical phonon.

Then, the total scattering rate of a state **k** for each scattering mechanism can be obtained as follows:

$$\frac{1}{\tau(\epsilon(k))} = \sum_{k'} W_{\mathbf{kk}'} \tag{S9}$$

b. Two-dimensional polarizability

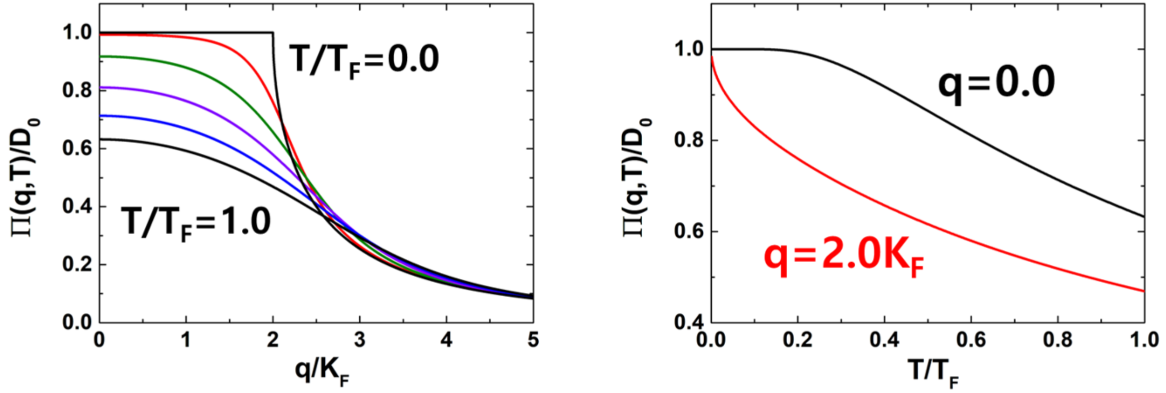

Figure S9. Two-dimensional polarizability Π(q,T) in units of the density of states at the Fermi level D_0.

In Fig. S9, we plot the corresponding polarizability $\prod(q,T)$ normalized by the density of states at Fermi level D_0. It shows strong wave vector and temperature dependences. Notably, in normal 2D systems, the $q = 2k_F$ scattering event is the most important for the electrical resistivity, and the strong temperature dependence of the polarizability function at $q = 2k_F$ leads to the anomalously strong temperature-dependent resistivity [S7].

c. Scattering rates and probability distributions for other scattering mechanisms

Other resulting 2D scattering rates, including the screening effect, are shown in Figs. S10–12 as a function of the carrier energy at T = 300 K. To account for the difference between the coupling matrix elements imposed by different phonons, the shown scattering rates are categorized by phonon-absorption and phonon-emission separately, as well as the angle-dependent probability distribution of the scattered state **k'** with initial carrier energy E = 0.04 and 0.1 eV. The different lines in each figure represent the results calculated from carrier concentrations: 0 (black), 1 (green), 10 (blue), and 100 (red) $\times 10^{10}$ cm^{-2}).

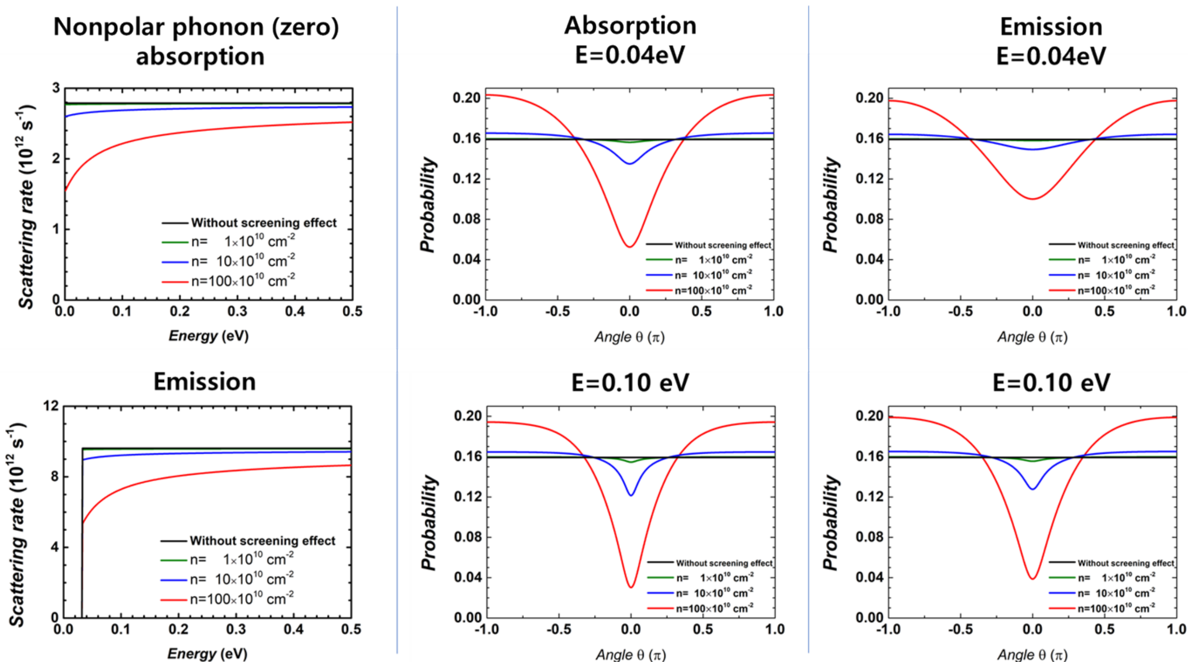

Figure S10. (Left) Zero-order nonpolar optical phonon scattering rates for the different carrier concentrations as a function of the carrier energy at T = 300 K (deformation potential = 5×10^8 eV/cm). Probability distribution of the scattered state k' as a function of angle with initial carrier energy E = 0.04 (middle) and 0.1 eV (right).

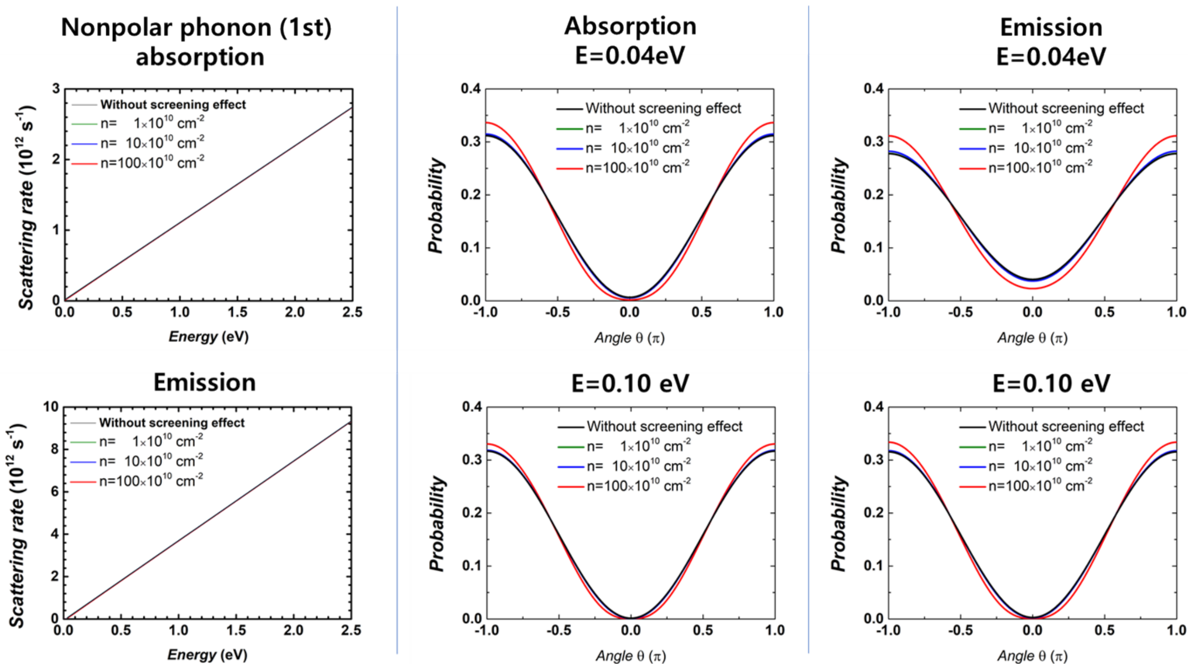

Figure S11. (Left) First-order nonpolar optical phonon scattering rates for the different carrier concentrations as a function of the carrier energy at T = 300 K (deformation potential = 5 eV). Probability distribution of the scattered state k' as a function of angle with initial carrier energy E = 0.04 (middle) and 0.1 eV (right).

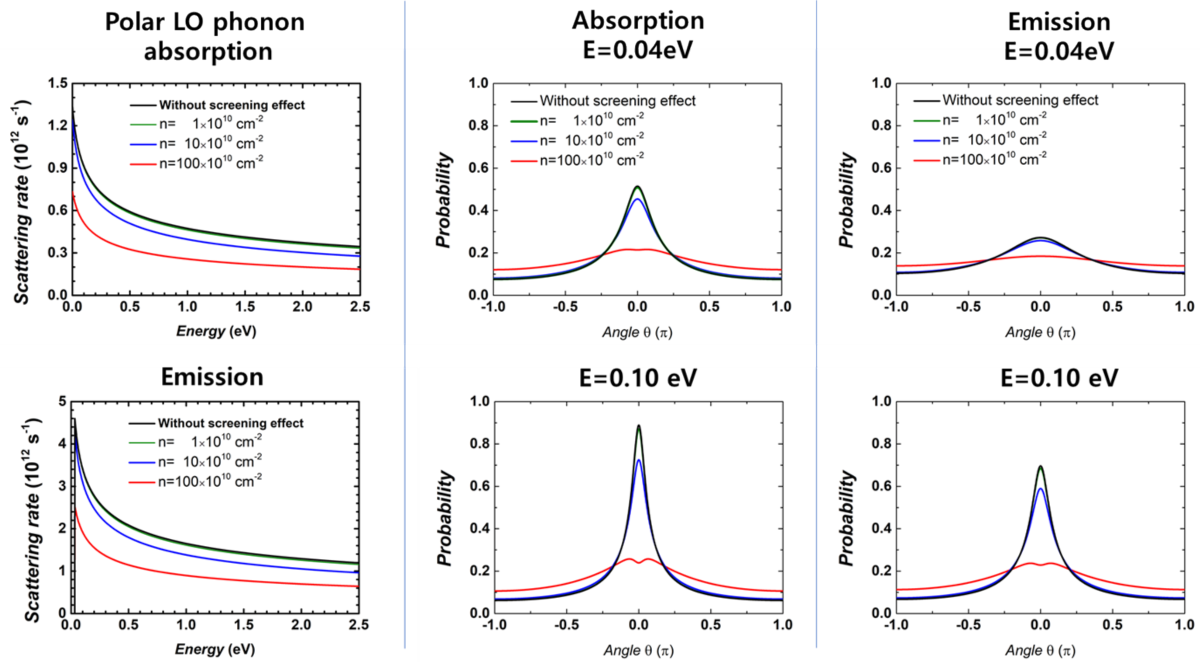

Figure S12. (Left) Polar LO phonon scattering rates for the different carrier concentrations as a function of the carrier energy at T = 300 K. Probability distribution of the scattered state k' as a function of angle with initial carrier energy E = 0.04 (middle) and 0.1 eV (right).

d. Excluding the effect of carrier–carrier scattering

The other potential reason for carrier density-dependent avalanche multiplication is carrier–carrier scattering. This two-body interaction cannot relax momentum or energy gained from the field because their collisions conserve both quantities. However, it can redistribute them over the carrier states. As mentioned above, our avalanche breakdown is dominated by polar LO phonons; the variation with energy-dependent scattering rate is significant only at the emission threshold ($h\omega_0$ = 32 meV). This suggests that notable effects primarily arise from the less frequent carrier–carrier

collisions, particularly those involving at least one carrier with energy exceeding $h\omega_0$ [S8]. To analyze these events, we employ an estimate of the collision rate for such processes, disregarding the effects of screening.

$$W_{ee} = (2\pi n)^{\frac{1}{2}} v(\hbar\omega_0) f_0(\hbar\omega_0) \quad \text{(S10)}$$

where n denotes the electron concentration, $v(\hbar\omega_0)$ denotes the velocity of carriers at the phonon energy, and f_0 denotes the Fermi–Dirac distribution function.

Eq. (S10) indicates that the carrier–carrier scattering rate is proportional to carrier density, which is plotted in Fig. S13. Due to relatively small optical phonon energy (32 meV) and high temperatures (300 K), its scattering rate is quite small (an order of magnitude of 10^9 s^{-1}) when compared with phonon scattering. Additionally, small momentum changes are favored for carrier–carrier scattering [S8]. Therefore, it has a minimal impact on hot carrier transport, insufficient to significantly delay the carrier from reaching the impact ionization threshold energy.

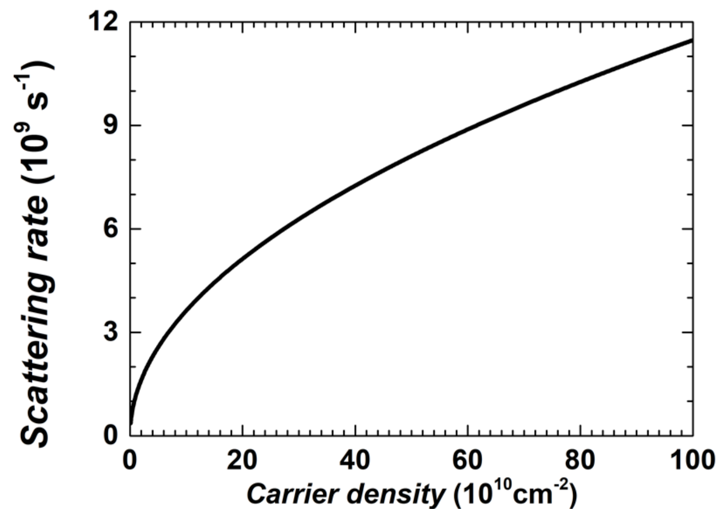

Figure S13. Carrier–carrier scattering rates as a function of carrier density at T = 300 K.

Supplementary Section 4. Photodetection via impact ionization

a. Photo-responsive characteristics based on carrier type

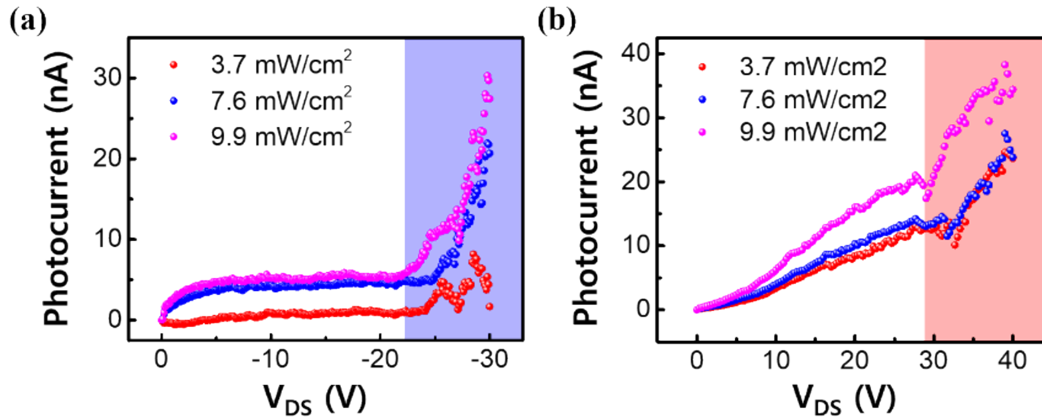

Figure S14. Photocurrent of **(a)** hole-initiated and **(b)** electron-initiated impact ionization under the same carrier densities for various laser intensities.

Figures S14a and b display the photocurrent measurements for both hole-initiated and electron-initiated impact ionization under various laser intensities, with each set corresponding to the same carrier density. The photocurrent exhibits a gradual increase with an applied bias smaller than V_{BR}, followed by a sharp increase as the bias exceeds V_{BR}, indicative of the respective carrier-initiated impact ionization processes. Under identical conditions, represented by circles of the same color, the hole-initiated impact ionization demonstrates higher photocurrent and a lower breakdown voltage compared to its electron-initiated counterpart.

b. Carrier density dependent photodetection

Figure S15 illustrates the effect of gate bias on the sudden increase in drain current, triggered by impact ionization in the WSe_2 channel. Figure S15a presents the I_{DS}-V_{DS} characteristics of the WSe_2 FET at various gate voltages (V_{GS}), where V_{GS} was incrementally decreased from –15 V (the charge neutral point for this device) to –30 V. Figure S15b displays the photocurrent as a function of carrier density, corresponding to the data in Fig. S15a. Although photocurrent levels are higher at greater carrier densities, impact ionization is more efficient at lower carrier densities. This is inferred from the comparison of the increase in photocurrent level relative to the saturation photocurrent under these conditions.

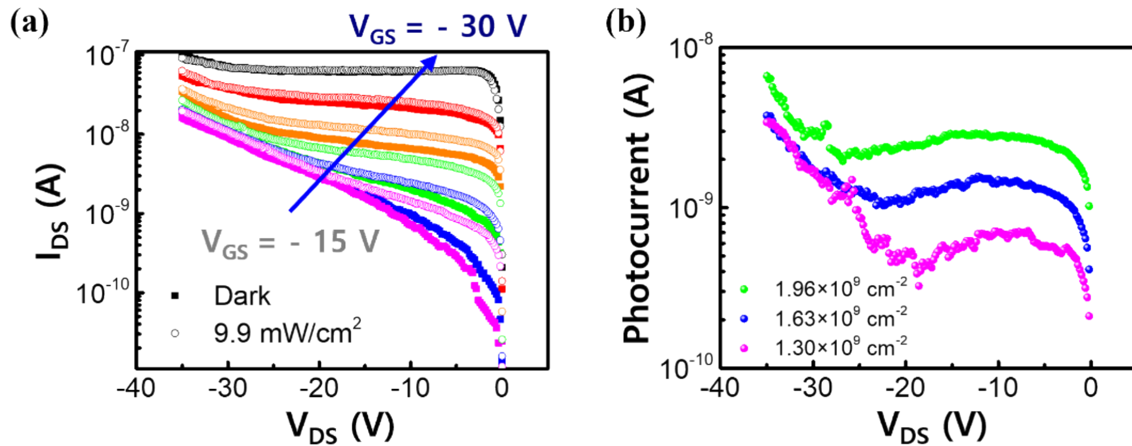

Figure S15. (a) Photo-excited I_{DS}–V_{DS} characteristics of the WSe_2-based APD at different gate voltages. **(b)** Calculated photocurrent as a function of drain voltage and electric field.

c. Photodetection by optimized impact ionization

Figure S16 shows the photocurrents with respect to the optimized impact ionization condition under light illuminations with different wavelengths. As the wavelength increases, the photocurrent decreases, but the V_{BR} becomes smaller, and a detectable photocurrent level is achieved due to significant impact ionization. This indicates the possibility of detecting a wide range of light up to a long wavelength of 1310 nm by amplifying a small photocurrent via optimized impact ionization.

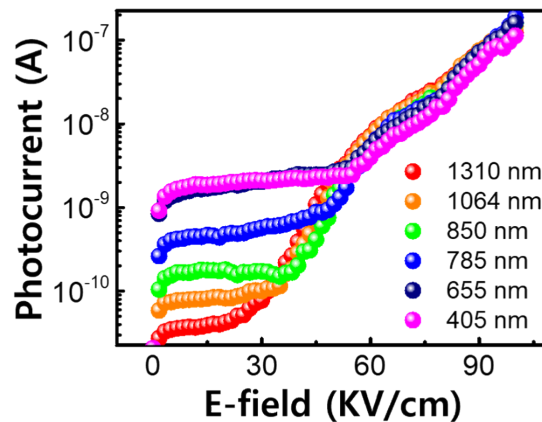

Figure S16. Measured photocurrent under the optimized condition (Low carrier density: V_{GS} = V_{CNP}; Hole-initiated impact ionization: $V_{DS} < 0$) versus the electric field.

d. Parameters for evaluating the performance of APD

Photoresponsivity (R) serves as a measure of the photocurrent generated per unit of incident irradiation, with a higher responsivity indicating greater detection capabilities at lower power levels. Detectivity (D^*) gauges the detector's ability to differentiate a signal from background noise, considering both the noise level of the incident irradiation and the dark current. External quantum efficiency (EQE) quantifies the number of photoinduced carriers generated for each incident photon. The signal-to-noise ratio *(SNR)* is the ratio of signal power to the variance induced by noise. Typically, R, D^*, EQE, and SNR are defined by the following equations (S11)–(S14):

$$R = \frac{I_{ph}}{P} \tag{S11}$$

(I_{ph}: photocurrent, P: intensity of the incident light)

$$D^* = \frac{(A\Delta f)^{1/2}}{NEP} \approx \frac{A^{1/2}R}{\sqrt{2eI_{dark}}} \tag{S12}$$

(A: detection area, I_{dark}: dark current, e: elementary charge)

$$EQE = \frac{I_{ph}hc}{Pe\lambda} = R\frac{hc}{e\lambda} \tag{S13}$$

(h: Planck constant, c: speed of light, λ: wavelength of the light)

$$SNR = \frac{{I_{ph}}^2}{\sigma^2} \ (\sigma^2 = 2e \times I_{dark} \times BW \times M^2, BW \approx \frac{1}{RT}) \tag{S14}$$

(BW: bandwidth, M: Multiplication factor, RT: Response time)

The calculated detectivity and S/N ratio as a function of the electric field are shown in Figs. S17a and b. (See Figure 4f for responsivity and external quantum efficiency.) We obtained a detectivity over 10^{11} and an S/N ratio of approximately 80.

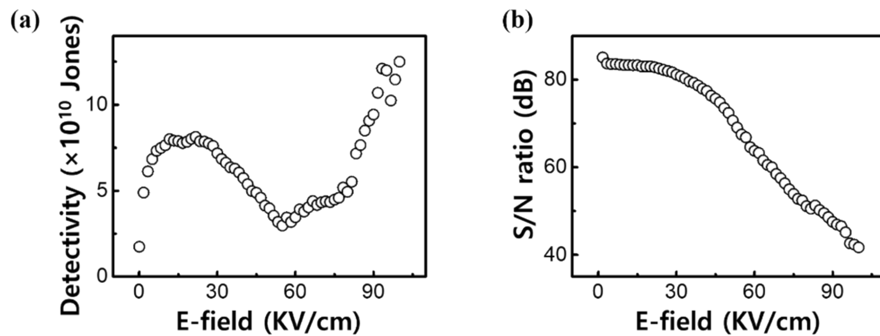

Figure S17. Calculated **(a)** detectivity and **(b)** signal-to-noise ratio versus electric field of WSe_2-

based APD.

Table S1. Comparison of photodetection performance with other WSe_2-based photodetectors and other 2D material-based avalanche photodetectors.

Detector type	EQE (%)	R (A/W)	D^* (Jones)	SNR	Wavelength	Ref
WSe_2-based PD						
WSe_2 PD	40	7	10^{14}	-	532 nm	[S9]
Gr-WSe_2-Gr PD	7.3	0.02	10^{10}	-	759 nm	[S10]
Gr-WSe_2 PD	-	7.55	10^{12}	-	532 nm	[S11]
WSe_2/GaSe PD	1490	6.2	-	-	520 nm	[S12]
n-doped WSe_2 PD	-	10^6	-	-	532 nm	[S13]
Gr-WSe_2-Gr PD	-	1.1	-	-	532 nm	[S14]
p-doped WSe_2 PD	-	364	10^{10}	-	520–850 nm	[S15]
WSe_2 PD	-	10^5	10^{14}	-	650 nm	[S16]
2D-based APD						
BP APD	2.719	1.16	-	-	532 nm	[S17]
BP-Au.NPs APD	382	160	-	350	520 nm	[S18]
BP/InSe APD (at low Temp.)	24.8	80	-	-	4 um	[S19]
InSe APD	11.1	4.86	-	62	543 nm	[S20]
MoS_2 APD	10^9	10^7	10^{16}	-	520 nm	[S21]
MoS_2/Si APD	4.31	2.2	-	-	633 nm	[S22]
$MoTe_2$-WS_2-$MoTe_2$ APD	14.1	6.02	-	71	400–700 nm	[S23]
This Work	10^4	10^2	10^{11}	85	405 nm	

Supplementary References

[S1] Marie, X.; Balkan, N. Springer Science & Business Media, 2012.

[S2] Shimizu, R.; Ze-Jun, D. *Rep. Prog. Phys.* 1992, **55**, 487.

[S3] Jin, Z.; Li, X.; Mullen, J. T.; Kim, K. W. *Phys. Rev. B* 2014, **90**, 045422.

[S4] Kawamura, T.; Sarma, S. D. *Phys. Rev. B* 1992, **45**, 3612.

[S5] Laturia, A.; Van de Put, M. L.; Vandenberghe, W. G. *npj 2D Mater. Appl.* 2018, **2**, 6.

[S6] Kaasbjerg, K.; Thygesen, K. S.; Jacobsen, K. W. *Phys. Rev. B* 2012, **85**, 115317.

[S7] Sarma, S. D.; Hwang, E. *Solid state commun.* 2005, **135**, 579-590.

[S8] Ridley, B. K. Oxford University Press, USA, 2013.

[S9] Pradhan, N. R.; Ludwig, J.; Lu, Z.; Rhodes, D.; Bishop, M. M.; Thirunavukkuarasu, K.; McGill, S. A.; Smirnov, D.; Balicas, L. *ACS Appl. Mater. Interfaces* 2015, **7**, 12080-12088.

[S10] Massicotte, M.; Schmidt, P.; Vialla, F.; Schädler, K. G.; Reserbat-Plantey, A.; Watanabe, K.; Taniguchi, T.; Tielrooij, K.-J.; Koppens, F. H. *Nat. Nanotechnol.* 2016, **11**, 42-46.

[S11] Zhou, C.; Zhang, S.; Lv, Z.; Ma, Z.; Yu, C.; Feng, Z.; Chan, M. *npj 2D Mater. Appl.* 2020, **4**, 46.

[S12] Wei, X.; Yan, F.; Lv, Q.; Shen, C.; Wang, K. *Nanoscale* 2017, **9**, 8388-8392.

[S13] Jo, S. H.; Kang, D. H.; Shim, J.; Jeon, J.; Jeon, M. H.; Yoo, G.; Kim, J.; Lee, J.; Yeom, G. Y.; Lee, S. *Adv. Mater.* 2016, **28**, 4824-4831.

[S14] Chen, J.; Liu, B.; Liu, Y.; Tang, W.; Nai, C. T.; Li, L.; Zheng, J.; Gao, L.; Zheng, Y.; Shin, H. S. *Adv. Mater.* 2015, **27**, 6722-6727.

[S15] Kang, D. H.; Kim, M. S.; Shim, J.; Jeon, J.; Park, H. Y.; Jung, W. S.; Yu, H. Y.; Pang, C. H.; Lee, S.; Park, J. H. *Adv. Funct. Mater.* 2015, **25**, 4219-4227.

[S16] Zhang, W.; Chiu, M.-H.; Chen, C.-H.; Chen, W.; Li, L.-J.; Wee, A. T. S. *ACS Nano* 2014, **8**, 8653-8661.

[S17] Atalla, M. R.; Koester, S. J. *75th Annual Device Research Conference (DRC)*, 2017; IEEE: pp 1-2.

[S18] Jia, J.; Jeon, J.; Park, J. H.; Lee, B. H.; Hwang, E.; Lee, S. *Small* 2019, **15**, 1805352.

[S19] Gao, A.; Lai, J.; Wang, Y.; Zhu, Z.; Zeng, J.; Yu, G.; Wang, N.; Chen, W.; Cao, T.; Hu, W. *Nat. Nanotechnol.* 2019, **14**, 217-222.

[S20] Lei, S.; Wen, F.; Ge, L.; Najmaei, S.; George, A.; Gong, Y.; Gao, W.; Jin, Z.; Li, B.; Lou, J. *Nano Lett.* 2015, **15**, 3048-3055.

[S21] Seo, J.; Lee, J. H.; Pak, J.; Cho, K.; Kim, J. K.; Kim, J.; Jang, J.; Ahn, H.; Lim, S. C.; Chung, S. *Adv. Sci.* 2021, **8**, 2102437.
[S22] Lopez-Sanchez, O.; Dumcenco, D.; Charbon, E.; Kis, A. *arXiv preprint arXiv*:1411.3232 2014.
[S23] Ouyang, T.; Wang, X.; Liu, S.; Chen, H.; Deng, S. *Front. Mater.* 2021, **8**, 736180.